

# Radio-Frequency Method for Investigation of Quantum Properties of Superconducting Structures

E. Il'ichev,<sup>1,\*</sup> A.Yu. Smirnov,<sup>2</sup> M. Grajcar,<sup>3</sup> A. Izmalkov,<sup>1,4</sup> D. Born,<sup>1,5</sup>  
N. Oukhanski,<sup>1</sup> Th. Wagner,<sup>1</sup> W. Krech,<sup>5</sup> H.-G. Meyer,<sup>1</sup> and A. Zagoskin<sup>2,6</sup>

<sup>1</sup>*Institute for Physical High Technology, P.O. Box 100239, D-07702 Jena, Germany*

<sup>2</sup>*D-Wave Systems Inc., 320-1985 W. Broadway, Vancouver, B.C., V6J 4Y3, Canada*

<sup>3</sup>*Department of Solid State Physics, Comenius University, SK-84248 Bratislava, Slovakia*

<sup>4</sup>*Moscow Engineering Physics Institute (State University), Kashirskoe sh. 31, 115409 Moscow, Russia*

<sup>5</sup>*Friedrich Schiller University, Institute of Solid State Physics, D-07743 Jena, Germany*

<sup>6</sup>*Physics and Astronomy Dept., The University of British Columbia,  
6224 Agricultural Rd., Vancouver, B.C., V6T 1Z1 Canada*

(Dated: November 10, 2018)

We implement the impedance measurement technique (IMT) for characterization of interferometer-type superconducting qubits. In the framework of this method, the interferometer loop is inductively coupled to a high-quality tank circuit. We show that the IMT is a powerful tool to study a response of externally controlled two-level system to different types of excitations. Conclusive information about qubits is obtained from the read-out of the tank properties.

PACS numbers: 74.50.+r , 85.25.-j

## I. INTRODUCTION

Quantum effects in mesoscopic superconducting circuits of small Josephson junctions have attracted renewed attention. It was clearly demonstrated that Josephson devices can behave like single microscopic particles if they are sufficiently isolated from the environment. Therefore, ideas developed in atomic and molecular physics can be used for description of artificially fabricated circuits of macroscopic size. These concepts are stimulated further by the perspectives of a promising way to realize quantum bits (qubits) for quantum information processing.

Qubits are two-level quantum systems with externally controlled parameters. Generally, two kinds of such devices with small-size Josephson junctions have been developed. One approach is based on charge degree of freedom, basis states of this kind of qubits are distinguished by the number of Cooper-pairs on a specially designed island. The alternative realization utilizes the phase of a Josephson junction (or the flux in a ring geometry), which is conjugate to the charge degree of freedom. Due to macroscopic size of superconducting qubits, they are extremely sensitive to external disturbances. Thus, a backaction of a detector should be as small as possible. A lot of different detectors have been suggested in literature (see Ref. 1 and references therein).

In this paper we review our results obtained on superconducting qubits by the impedance measurement technique (IMT). Below we shall discuss several quantum effects including macroscopic quantum tunneling, Landau-Zener transitions, Rabi oscillations, and direct resonant spectroscopy of the qubit energy levels. Finally, we present our very recent results of investigation of two coupled qubits.

## II. MACROSCOPIC QUANTUM TUNNELING

For the flux qubits the Josephson energy dominates over the charge energy,  $E_J \gg E_C$ . It was predicted, that such systems should exhibit various quantum-mechanical effects including macroscopic quantum tunneling (MQT) of the flux.<sup>2</sup> Indeed, predicted effects had been observed experimentally.<sup>3,4,5,6</sup> In this section we briefly discuss the main properties of the flux qubits and demonstrate that the IMT technique is a powerful tool for the investigation of the MQT.

One of the realizations of the flux qubit is a superconducting loop with low inductance  $L_q$ , including three Josephson junctions (a 3JJ qubit).<sup>7</sup> Its total Josephson energy is  $E_J = \sum_{i=1}^3 E_{J_i}(\phi_i)$ , where  $\phi_i$  and  $E_{J_i} = \hbar I_{c_i}/2e$  are the phase difference and Josephson energy of the  $i$ th junction, respectively. Due to flux quantization, only  $\phi_{1,2}$  are independent with  $\phi_3 = -\phi_1 - \phi_2 - 2\pi\Phi_e/\Phi_0$  ( $\Phi_0 = h/2e$  is the flux quantum) for negligibly small  $L_q$  (though see<sup>8</sup>).

At  $\Phi_e = \frac{1}{2}\Phi_0$ , the potential  $U(\phi_1, \phi_2)$  has two shallow minima. These two minima correspond to the qubit states  $\psi_L$  and  $\psi_R$ , carrying opposite but equal supercurrents around the loop. Therefore, according to the laws of quantum mechanics, near degeneracy the system can tunnel between the two potential minima.

In the basis  $\{\psi_L, \psi_R\}$  and near  $\Phi_e = \frac{1}{2}\Phi_0$ , the flux qubit can be described by the Hamiltonian

$$H = -\frac{\Delta}{2}\sigma_x - \frac{\varepsilon}{2}\sigma_z. \quad (1)$$

At bias  $\varepsilon = 0$ , the two lowest levels of the qubit anticross (Fig. 1a) with energy gap  $\Delta$ . With  $\varepsilon$  changing sign, the qubit can either adiabatically transform from  $\psi_L$  to  $\psi_R$  staying in the ground state  $E_-$  or switch to the excited state  $E_+$ . The probability of the latter (called

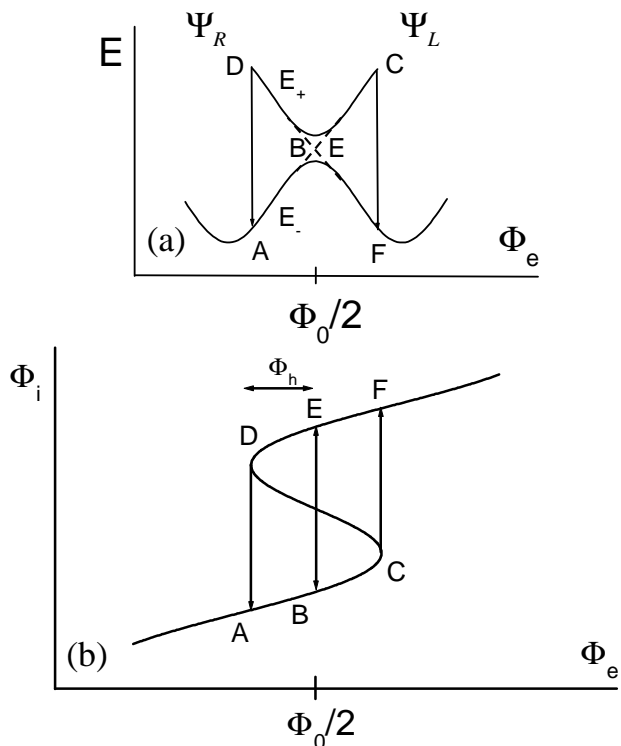


FIG. 1: (a) Quantum energy levels of the 3JJ flux qubit vs external flux. The dashed lines correspond to the classical potential minima. In all graphs, the states A, B, C correspond to, say,  $\Psi_L$  with left-rotating supercurrent. As  $\Phi_e$  is increased, these lose classical stability in favour of the corresponding states  $\Psi_R$ , denoted by D, E, and F. (b) Internal vs external qubit flux.

Landau-Zener transition) for linear sweep  $\varepsilon(t) = vt$  and  $\varepsilon$  changing from  $-\infty$  to  $\infty$  was calculated<sup>9</sup> to be  $P_{LZ} = \exp(-\pi\Delta^2/2\hbar v)$ .

In order to demonstrate the principle of the IMT measurements of this system, let us consider the internal flux representation (Fig. 1b) instead of the energy one (Fig. 1a). A similar picture is usually used for the explanation of the operation of the conventional radio-frequency (rf) SQUID. The main difference between an rf SQUID and a qubit behavior is the existence of the adiabatic trajectory  $BE$  for latter one (see Fig. 1a, b). Let us assume that  $BE$  trajectory is forbidden and “qubit” is inductively coupled to the high-quality resonant circuit. Then the system exhibits hysteretic behavior.<sup>10</sup> The tank circuit is simultaneously driven by a dc bias current  $I_{dc}$  and an ac current  $I_{rf}$  of a frequency  $\omega$  close to the resonance frequency of the tank circuit. Both currents produce the total magnetic flux applied to the qubit  $\Phi_e = \Phi_{dc} + \Phi_{rf} \cos \omega t$ . If the amplitude  $\Phi_{rf} > \Phi_h$ , where  $\Phi_h$  is the half-width of the hysteresis loop  $ACFD$  (Fig. 1b), the tank circuit will register the energy losses proportional to the loop area, as long as  $|\Phi_{dc} - \frac{1}{2}\Phi_0| < \Phi_{rf} - \Phi_h$ . These losses occur due to the jumps from  $E_+$  to  $E_-$  at the ends of the loop. This idea was used by A. Silver and J. Zimmerman to

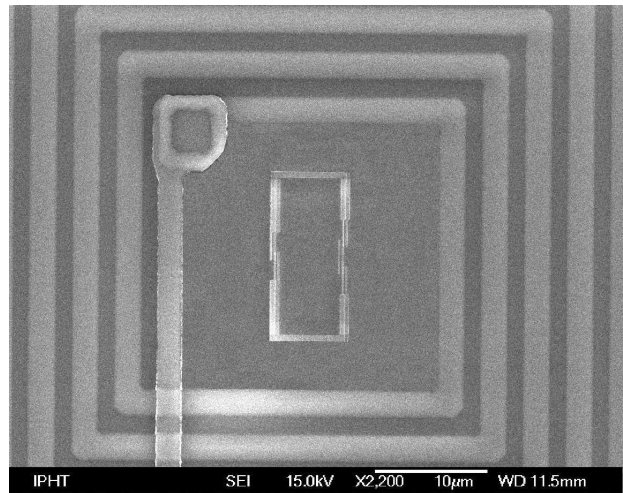


FIG. 2: Electron micrograph of the qubit at the center of the tank coil.

build the first rf SQUID magnetometers.<sup>11</sup> If  $\Phi_{rf} > \Phi_h$  the rf voltage across the tank circuit is a  $\Phi_0$ -periodical function of applied dc flux  $V_T(\Phi_{dc})$  with local minima at  $\Phi_{dc} = \frac{1}{2}\Phi_0 + n\Phi_0$ , where  $n$  is integer.

Now, let us take into account the additional “quantum” trajectory  $BE$  (see Fig. 1b). If its probability  $1 - P_{LZ}$  is nonzero but less than 1, two new closed paths  $ABED$  and  $BCFE$  are possible. There are two contributing trajectories, adiabatic and Landau-Zener transition. Therefore the net dissipation is  $P_{loss} = 2P_{LZ}(1 - P_{LZ})$  and vanishes if  $P_{LZ}$  is either too small or too large<sup>13</sup>. Due to the exponential dependence of  $P_{LZ}$  on the sweep rate, in practice this makes the *quantum* losses observable only if the bias sweep narrowly overshoots the anticrossing, i.e., if

$$|\Phi_{dc} - \frac{1}{2}\Phi_0| \lesssim \Phi_{rf}, \quad (2)$$

when  $\Phi_e$  changes slowly. Plotting  $V_T(\Phi_{dc})$  for  $\Phi_{rf} > \Phi_h/2$ , a plateau flanked by two peaks is expected. The position of the dips depends on  $\Phi_{rf}$  as follows from Eq. 2. Therefore in contrast to  $V_T(\Phi_{dc})$  dependence of an rf SQUID the qubit should exhibit two local minima (in one period) which are symmetrical with respect to  $\Phi_{dc} = \frac{1}{2}\Phi_0$ . For the amplitude  $\Phi_{rf} > \Phi_h$  the  $ACFD$  hysteresis becomes closed as well. Here, similar to the rf SQUID, on the  $V_{rf}(\Phi_{dc})$  dependence should appear the local minimum exactly at  $\Phi_{dc} = \frac{1}{2}\Phi_0$ . Note, that  $\Phi_e$  here plays a role of bias  $\varepsilon$  for the Hamiltonian (1).

To test the ideas discussed above, we prepared lithographically square-shaped Nb pancake coils with inductance  $L_T$  on oxidized Si substrates for the tank circuits. We used an external capacitance  $C_T$  to be able to change the resonant frequency  $\omega_T = 1/\sqrt{L_T C_T}$ . The line width of the 30 coil windings was  $2 \mu\text{m}$ , with a  $2 \mu\text{m}$  spacing. The quality factor of the tank was  $Q_T \approx 1500$  at  $\omega_T \sim 20 \text{ MHz}$ . The 3JJ qubit structure was fabricated out of Al in the middle of the coil by conventional

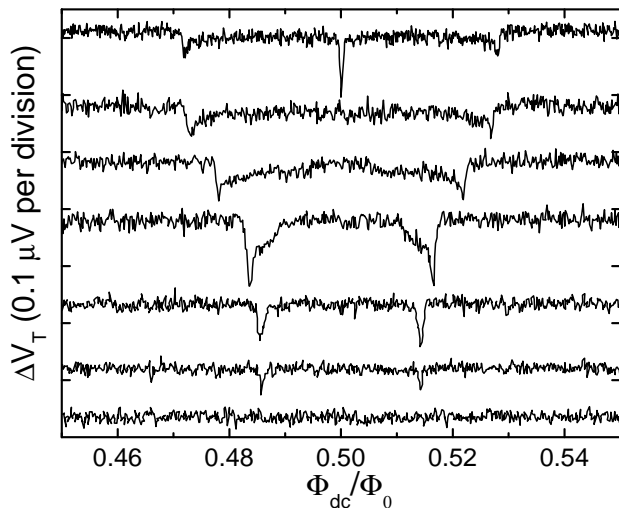


FIG. 3: Tank voltage vs. magnetic flux bias near the degeneracy point of the qubit  $\frac{1}{2}\Phi_0$ . From the lower to upper curve, the driving voltage is 10.2, 10.7, 11.2, 13.1, 17.2, 21.3, 22.0  $\mu\text{V}$  rms (data vertically shifted for clarity).

shadow evaporation technique. The Josephson junctions with critical current density  $j_c \approx 300\text{A}/\text{cm}^2$  have areas  $\approx 130 \times 620 \text{ nm}^2$ ,  $120 \times 600 \text{ nm}^2$ , and  $110 \times 610 \text{ nm}^2$  respectively. The loop area was  $90 \mu\text{m}^2$ , with  $L_q = 39 \text{ pH}$ . The fabricated structure is shown in Fig. 2.

We measured  $V_T(\Phi_{dc})$  by a three-stage cryogenic amplifier placed at  $\approx 2 \text{ K}$ .<sup>12</sup> Results for small driving voltage are shown in Fig. 3. For the smallest voltages no dissipative response is observed; the two “quantum” peaks appear around  $10.7 \mu\text{V}$ ,<sup>13</sup> and subsequently move apart without significant broadening. The “classical” peak appears in the center, and with an ac bias threshold *double* the one of the quantum peaks—both as predicted above.

Now assume that the probability of a Landau-Zener transition is small and the qubit adiabatically changes from  $\psi_L$  to  $\psi_R$ , always staying in the ground state  $E_-$ . This means that the hysteresis *ACFD* is “shunted” by the *BE* trajectory. Therefore there are no losses caused by the flux jumps in the qubit. However, in the vicinity of *B* (see Fig. 1b) the small change of the external magnetic flux causes a considerable change of the flux inside the qubit. Due to coupling of the qubit to the tank, the effective inductance of the tank-qubit system is changed, which leads to the change of the resonant frequency. In this context the convenient measure of that change is the imaginary part of the total impedance<sup>14</sup> expressed through the phase angle  $\chi$  between driving current  $I_{bias}(t) = I_{ac} \cos \omega t$ , and tank voltage  $V_T(t) = V_T \cos(\omega t + \chi)$ . For small  $L_q$  and if the amplitude of  $I_{rf}$  is negligible, the results are summarized by<sup>15</sup>

$$\tan \chi = k^2 Q_T L_q \frac{d^2 E_-(f_x)}{d\Phi_e^2}, \quad (3)$$

where  $k = M/\sqrt{L_q L_T}$  is the tank-qubit coupling co-

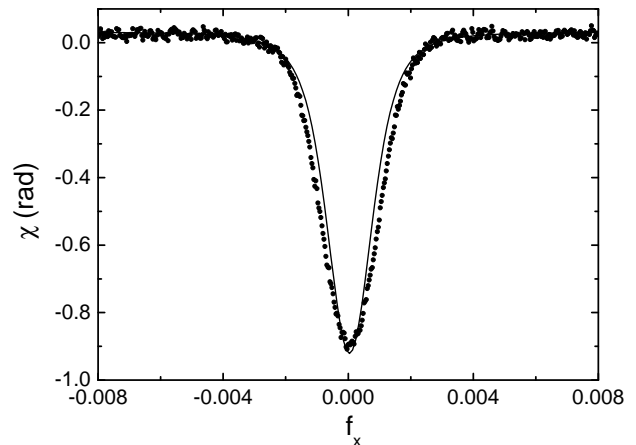


FIG. 4: Tank phase shift vs. flux bias near degeneracy  $f_x = 0$ . Dots correspond to experimental data, solid line is the theoretical fit with  $\Delta/h = 650 \text{ MHz}$ .

efficient, with  $M$  being the mutual inductance between them. The ground-state curvature is<sup>15</sup>

$$\frac{d^2 E_-}{d\Phi_e^2} = -\frac{E_J^2 \Delta^2 \lambda^2}{\Phi_0^2 (4E_J^2 \lambda^2 f_x^2 + \Delta^2)^{3/2}}, \quad (4)$$

where

$$f_x = \frac{\Phi_e}{\Phi_0} - \frac{1}{2}, \quad (5)$$

and  $\lambda$  is the normalized flux-to-energy conversion factor. Since all quantities in Eqs. (3)–(5) can be measured independently, experimental results can be compared with theoretical expectations.<sup>16</sup>

Strictly speaking, Eq. (3) describes a measurement of the quantum object with vanishing back-action. Therefore, its validity should be proved.<sup>17</sup> Taking into account the influence of the tank on the qubit, the Hamiltonian (1) should be rewritten as:

$$H = -\frac{\Delta}{2}\sigma_x - \frac{\varepsilon}{2}\sigma_z - \sigma_z(Q_0 + f + \gamma \hat{I}_T) + H_T + H_{qB}, \quad (6)$$

where  $\gamma = I_q M$  is the coupling coefficient between the qubit’s current,  $\hat{I}_q = I_q \sigma_z$ , and the current in the tank  $\hat{I}_T$ . An infinitesimally small auxiliary force  $f(t)$  is required for calculations of qubit’s magnetic susceptibility. A heat bath operator  $Q_0$  and a Hamiltonian  $H_{qB}$  describe internal mechanisms of dissipation and fluctuations in the superconducting loop. The high-quality tank is treated here as a quantum cavity is characterized by creation/annihilation photon operators  $a^+$ ,  $a$  which obey the Bose commutation rules  $[a, a^+]_- = 1$  etc. Quantum-mechanical operators of a current and a voltage in the tank are defined as:  $\hat{I}_T = \sqrt{\hbar\omega_T/2L_T}(a + a^+)$ ,  $\hat{V}_T = i\sqrt{\hbar\omega_T/2C_T}(a^+ - a)$ . For the Hamiltonian of the tank driven by a bias current  $I_{bias}$  and coupled to its own heat

bath  $Q_b$  we get the expression

$$H_T = \hbar\omega_T(a^\dagger a + 1/2) - (a + a^\dagger)Q_b - L_T \hat{I}_T I_{bias} + H_{TB}. \quad (7)$$

The internal heat bath of the tank  $Q_b$ , characterized by a free Hamiltonian  $H_{TB}$ , results in a finite life time of the photons,  $\gamma_T^{-1}$ , and, because of this, in a finite quality factor,  $Q_T = \omega_T/\gamma_T$ . Assuming that  $\hbar = 1, k_B = 1$ , we derive the Heisenberg equations for the tank operators:  $\dot{\hat{I}}_T = \hat{V}_T/L_T$ , and

$$\left(\frac{d^2}{dt^2} + \gamma_T \frac{d}{dt} + \omega_T^2\right) \hat{V}_T = \xi_b + \lambda\omega_T^2 \dot{\sigma}_z + \frac{1}{C_T} \dot{I}_{bias}, \quad (8)$$

where  $\xi_T(t)$  is a fluctuation source with zero average value,  $\langle \xi \rangle = 0$ , and a correlator,  $\langle \xi_b(\omega)\xi_b \rangle$ , which is proportional to the linewidth of the tank  $\gamma_T$  and the tank temperature  $T$ :  $\langle \xi_b(\omega)\xi_b \rangle = (2\gamma_T T/C_T)\omega^2$ . Because of inductive coupling the current and the voltage in the tank,  $\hat{I}_T$  and  $\hat{V}_T$ , affect the qubit current,  $\hat{I}_q = I_q \sigma_z$ . Using the linear response theory this influence can be presented as follows

$$\dot{\sigma}_z = \dot{\sigma}_{z,0} + \frac{\lambda}{L_T} \int dt_1 \langle \frac{\delta\sigma_z(t)}{\delta f(t_1)} \rangle \hat{V}_T(t_1) \quad (9)$$

where an operator  $\sigma_{z,0}$  describes fluctuations of the qubit current caused by its internal heat bath,  $Q_0$ , which is not correlated with the heat bath of the tank,  $Q_b$ . We also take into account relations  $(\delta/\delta I_T) = \lambda(\delta/\delta f)$  and  $\dot{\hat{I}}_T = \hat{V}_T/L_T$ .

The function  $\langle \delta\sigma_z(t)/\delta f(t_1) \rangle$  involved in Eq. (9) is proportional to the derivative of the qubit current  $I_q(t) = \langle \hat{I}_q \rangle$  over the flux  $\Phi_T = L_T I_T$  created by the tank,  $\delta I_q(t)/\delta \Phi(t_1)$ , or to the second derivative of the qubit energy profile,  $E(\Phi)$ , over the flux,  $\partial^2 E(\Phi)/\partial \Phi^2$  (compare with Eq. 3). It is convenient to characterize the qubit response on the action of the tank by means of the magnetic susceptibility<sup>18</sup>  $\chi_{zz}(\omega)$  defined as

$$\langle \frac{\delta\sigma_z(t)}{\delta f(t')} \rangle = \int \frac{d\omega}{2\pi} e^{-i\omega(t-t')} \chi_{zz}(\omega). \quad (10)$$

Then, the voltage in the tank obeys the equation

$$\int dt_1 \left[ \left( \frac{d^2}{dt^2} + \gamma_T \frac{d}{dt} + \omega_T^2 \right) \delta(t-t_1) - \frac{\lambda^2}{L_T} \omega_T^2 \langle \frac{\delta\sigma_z(t)}{\delta f(t_1)} \rangle \right] \hat{V}_T(t_1) = \xi_b + \lambda\omega_T^2 \dot{\sigma}_{z,0} + \lambda\omega_T^2 \frac{1}{C_T} \dot{I}_{bias}. \quad (11)$$

It is evident from this equation that the tank voltage contains information about the magnetic susceptibility  $\chi_{zz}(\omega)$  of the qubit. Similar to classical case this information can be extracted from measurements of the phase

angle  $\chi$ . It follows from the averaged Eq. (11) that amplitudes of harmonic oscillations of the tank voltage and the bias current are related through

$$V_T e^{-i\chi} = -i\omega \left\{ \omega_T^2 \left[ 1 - \frac{\lambda^2}{L_T} \chi'_{zz}(\omega) \right] - \omega^2 - i\omega \left[ \gamma_T + \frac{\lambda^2 \omega_T^2}{\omega L_T} \chi''_{zz}(\omega) \right] \right\}^{-1} \frac{I_{ac}}{C_T} \quad (12)$$

with  $\chi'_{zz}(\omega)$  and  $\chi''_{zz}(\omega)$  being the real and imaginary parts of the qubit magnetic susceptibility (10). In the case when the tank is driven exactly with the resonant frequency,  $\omega = \omega_T$ , the voltage amplitude,  $V_T$ , can be found from the equation:

$$V_T = \frac{I_{ac}}{C_T} \left\{ [k^2 L_q I_q^2 \omega_T \chi'_{zz}(\omega_T)]^2 + [\gamma_T + k^2 L_q I_q^2 \omega_T \chi''_{zz}(\omega_T)]^2 \right\}^{-1/2}, \quad (13)$$

whereas for the voltage-current phase shift we obtain the expression

$$\tan \chi = -2k^2 L_q I_q^2 \bar{Q}_T \chi'_{zz}(\omega_T). \quad (14)$$

Here  $\bar{Q}_T = \omega_T/(\bar{\gamma}_T)$  is an effective quality factor of the tank wherein a broadening of tank's line width,

$$\bar{\gamma}_T = \gamma_T + k^2 L_q I_q^2 \omega_T \chi''_{zz}(\omega_T), \quad (15)$$

due to the qubit is taken into account. The magnetic susceptibility of the qubit (Eq. 10) is calculated from the Bloch equations written in the form:

$$\begin{aligned} \langle \dot{\sigma}_x \rangle + \Gamma_x (\langle \sigma_x \rangle - \sigma_x^0) &= -\varepsilon \langle \sigma_y \rangle, \\ \langle \dot{\sigma}_y \rangle + \Gamma_y \langle \sigma_y \rangle &= -\Delta \langle \sigma_z \rangle + \varepsilon \langle \sigma_x \rangle - 2f \sigma_x^0, \\ \langle \dot{\sigma}_z \rangle &= \Delta \langle \sigma_y \rangle, \end{aligned} \quad (16)$$

where  $\Gamma_x$  and  $\Gamma_y$  are qubit's damping rates,  $\sigma_x^0 = -(\Delta/\omega_c) \tanh(\omega_c/2T)$  is a steady-state polarization of the qubit with energy splitting  $\omega_c = \sqrt{\Delta^2 + \varepsilon^2}$ , which is much higher than the resonant frequency of the tank,  $\omega_c \gg \omega_T$ . Because of this the decoherence and relaxation rates drop out of the expression for the magnetic susceptibility:

$$\begin{aligned} \chi_{zz}(\omega_T) &= \chi'_{zz}(\omega_T) = \\ &= 2 \frac{\Delta^2}{(\Delta^2 + \varepsilon^2)^{3/2}} \tanh\left(\frac{\sqrt{\Delta^2 + \varepsilon^2}}{2T}\right). \end{aligned} \quad (17)$$

As a result, the phase angle between the voltage in the tank and the bias current is given by the formula

$$\begin{aligned} \tan \chi &= -2k^2 \frac{L_q I_q^2}{\Delta} \bar{Q}_T \left( \frac{\Delta^2}{\Delta^2 + \varepsilon^2} \right)^{3/2} \\ &\quad \times \tanh\left(\frac{\sqrt{\Delta^2 + \varepsilon^2}}{2T}\right). \end{aligned} \quad (18)$$

By making use of simple algebra it can be shown that at  $T = 0$  Eqs. (3) and (18) are equivalent. Therefore, indeed measuring  $\tan \chi$  as a function of the bias applied to the qubit, let us to determine the qubit's tunneling rate  $\Delta$ .

In order to realize the adiabatic response of the qubit experimentally, we fabricated 3JJ Al qubit with the following parameters. The area of two, nominally equivalent junctions was about  $190 \times 650 \text{ nm}^2$  while one is smaller, so that  $\alpha \equiv E_{J3}/E_{J1,2} \approx 0.8$ . The value of the critical current for larger junction was determined to be  $I_c \approx 380 \text{ nA}$ . Qubit inductance, tank parameters, and measurement setup were the same as in the case of Landau-Zener transitions described above.

The measured  $\chi(f_x)$  curve at nominal mixing-chamber temperature  $T = 10 \text{ mK}$  is shown in Fig. 4. The curve was fitted by Eq. (3) with  $\Delta$  as a free parameter. Calculated curve for the best fit parameter  $\Delta/h = 650 \text{ MHz}$  is also shown Fig. 4. This value of energy gap was in good agreement with the gap determined independently from temperature measurements.<sup>16</sup>

### III. RABI SPECTROSCOPY

Quite generally, a two-level quantum system (including qubits), should exhibit coherent (Rabi) oscillations in time in the presence of resonant irradiation. Microwaves in resonance with the spacing between qubit's energy levels will cause their occupation probabilities to oscillate, with a frequency proportional to the microwave amplitude. Indeed, coherent oscillations between energy levels of the superconducting qubit were detected.<sup>19,20,21,22</sup>

In this section we show that the tank can be used for detection of Rabi oscillations as well. If the resonant microwave signal is applied, the phase-coherent oscillations of the level occupation will only last for a finite time, which is usually called the coherence time. The correlation between the occupations can be expressed by an autocorrelation function or its Fourier transform, the spectral density. For example for the IMT, when the flux qubit is coupled inductively to a tank circuit, the spectral density of the tank-voltage fluctuations rises above the background noise when the qubit's Rabi frequency  $\Omega_R$  coincides with the tank's resonant frequency  $\omega_T$ . This forms the basis for our measurement technique of *Rabi spectroscopy*. Rabi oscillations cause changes of the qubit's magnetic moment and, therefore, excite the tank. The tank circuit accumulates photons which were emitted by the qubit. This approach is similar to the one in entanglement experiments with Rydberg atoms and microwave photons in a cavity.<sup>23</sup>

Indeed, quantitative information can be extracted from the noise spectrum  $S_V(\omega)$  of the voltage fluctuations (the Fourier transform of the correlator  $M_V(t, t') = \langle (1/2)[\hat{V}_T(t), \hat{V}_T(t')]_+ \rangle$ ) in the tank,<sup>17</sup> which incorporates the noise spectrum of the tank,  $S_{VT}$ , supplemented by the qubit's contribution  $S_{VQ}$ ,  $S_V = S_{VT}(\omega) + S_{VQ}(\omega)$ ,

where

$$S_{VT}(\omega) = 2 \frac{\omega^2}{C_T} \frac{T\gamma_T}{(\bar{\omega}_T^2 - \omega^2)^2 + \omega^2\bar{\gamma}_T^2}. \quad (19)$$

The qubit's part of voltage noise can be found from the stochastic equation (11) for the tank voltage:

$$S_{VQ}(\omega) = \omega^2 \frac{\omega_T}{C_T} \times \frac{k^2 L_q I_q^2 \omega_T S_{zz}(\omega)}{(\bar{\omega}_T^2 - \omega^2)^2 + \omega^2\bar{\gamma}_T^2}. \quad (20)$$

Here  $S_{zz}(\omega)$  is a Fourier transform of the correlator  $\langle 1/2 [\sigma_{z,0}(t), \sigma_{z,0}(t')]_+ \rangle$ , which describes internal fluctuations in the qubit (not related to the tank). Hand in hand with the tank's damping rate,  $\bar{\gamma}_T$  (15), the resonance frequency of the tank,  $\bar{\omega}_T$ , is also shifted because of the qubit-tank interaction,

$$\bar{\omega}_T = \omega_T \sqrt{1 - k^2 L_q I_q^2 \chi'_{zz}(\omega_T)}. \quad (21)$$

The spectrum of voltage fluctuations has a peak near the resonant frequency of the tank  $\omega_T$ , and, therefore, it contains information about a low-frequency component  $S_{zz}(\omega_T)$  of the qubit spectrum. The equilibrium part of this spectrum peaks at the energy splitting  $\omega_c = \sqrt{\Delta^2 + \varepsilon^2}$  of the tunneling doublet which differs significantly from the frequency of the tank,  $\omega_c \gg \omega_T$ . Because of this, a contribution of equilibrium qubit noise to the voltage spectrum of the tank is expected to be negligibly small. An external microwave source with a frequency  $\omega_0$  tuned in resonance with the energy splitting of the qubit  $\omega_c$ , induces periodical variations of a population difference between the excited and ground state of the qubit, which are characterized by a frequency  $\Omega_R = \sqrt{(\Delta/\omega_c)^2 F^2 + \delta_0^2}$  depending on the amplitude  $F$  of the microwave source as well as on the detuning  $\delta_0 = \omega_0 - \omega_c$ . With non-zero bias,  $\varepsilon \neq 0$ , left and right wells of the qubit potential have different energies. As a consequence, Rabi oscillations between the energy eigenstates will be accompanied by low-frequency transitions of the qubit from the left to the right well and back. The tank detects this kind of low-frequency noise which is described by the Lorentzian spectrum centered at the Rabi frequency  $\Omega_R$  with a linewidth dependent on the qubit decoherence rate  $\Gamma$ . Both the tank ( $\Gamma_T$ ) and the internal heat bath ( $\Gamma_0$ ) contribute to the decoherence rate  $\Gamma$ ,  $\Gamma = \Gamma_0 + \Gamma_T$ . It should be emphasized that the external microwave field affects the qubit-bath coupling<sup>24</sup> that results in the distinction of the nonequilibrium decay rate  $\Gamma$  from its equilibrium counterparts  $\Gamma_x, \Gamma_y$  entering the Bloch equations (16).

An informative part of the spectrum of voltage fluctuations,  $S_{VQ}(\omega)$ , incorporates the qubit Lorentzian multiplied by the transmission function of the tank having a sharp peak at the frequency  $\omega_T$ :

$$S_{VQ}(\omega) = 2 \frac{\varepsilon^2}{\omega_c^2} k^2 \frac{L_q I_q^2}{C_T} \omega^2 \Gamma_0 \frac{\omega_T^2}{(\bar{\omega}_T^2 - \omega^2)^2 + \omega^2\bar{\gamma}_T^2} \times \frac{\Omega_R^2}{(\omega^2 - \Omega_R^2)^2 + \omega^2\Gamma^2}. \quad (22)$$

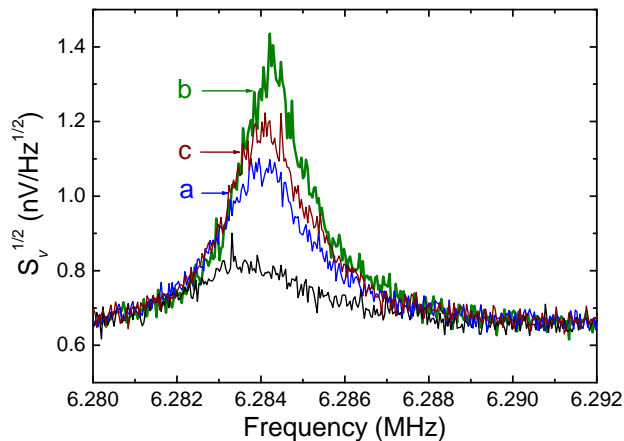


FIG. 5: The spectral noise amplitude of the tank voltage for UHF powers  $P_a < P_b < P_c$  at 868 MHz. The bottom curve corresponds to the background noise without an HF signal.

The linewidth of the tank is assumed to be much less than the qubit's damping rate,  $\gamma_T \ll \Gamma$ . Because of this, as a function of frequency  $\omega$ , the spectrum of voltage noise (22) represents a Lorentzian with a width  $\gamma_T$  and an amplitude which is given by a Lorentzian function of the Rabi frequency having the maximum near  $\omega_T$  and the width  $\Gamma$ . Measurements of the noise spectrum amplitude at different values of the microwave power  $P$  allow to extract information not only about the existence of Rabi oscillations, but also about the nonequilibrium decoherence rate  $\Gamma$  of the qubit. We note that due to strong nonequilibrium conditions the populations of the qubit's levels are practically equal, and the noise spectrum amplitude does not depend on the temperature. The signal-to-noise ratio,

$$\frac{S_{VQ}(\omega)}{S_{VT}(\omega)} \Big|_{\omega=\omega_T} = \frac{\varepsilon^2}{\omega_c^2} k^2 \frac{L_q I_q^2}{T} \frac{\Gamma_0}{\gamma_T} \times \frac{\omega_T^2 \Omega_R^2}{(\omega_T^2 - \Omega_R^2)^2 + \omega_T^2 \Gamma^2}, \quad (23)$$

peaks when  $\Omega_R = \omega_T$ . At the same point, the backaction of the measuring device (tank) on the quantum bit which is described by the damping rate  $\Gamma_T$ ,

$$\Gamma_T = 4k^2 L_q I_q^2 \frac{\varepsilon^2}{\omega_c^2} \omega_T^2 \frac{T \gamma_T}{(\omega_T^2 - \Omega_R^2)^2 + \Omega_R^2 \gamma_T^2}. \quad (24)$$

reaches its maximum as well. However, the tank contribution to the qubit decoherence drastically decreases with small detuning of the Rabi frequency  $\Omega_R$  from  $\omega_T \gamma_T \ll |\Omega_R - \omega_T| < \Gamma$ . At the same time, the efficiency of measurements,  $(S_{VQ}(\omega)/S_{VT}(\omega))|_{\omega=\omega_T}$ , remains practically unchanged. Since  $\Gamma \ll \Omega_R$ , the spectroscopic monitoring of Rabi oscillations with the low-frequency tank circuit falls into the category of weak continuous quantum measurements.

The measurement setup as well as sample fabrication were similar to the ones described in the previous section.

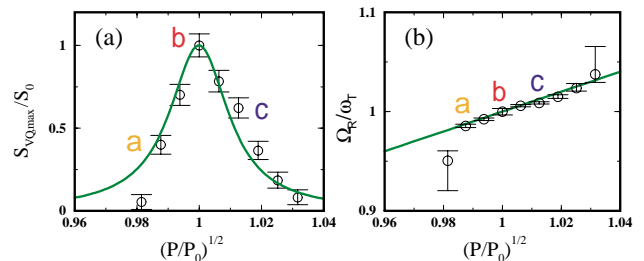


FIG. 6: (a) Comparing the data to the theoretical Lorentzian. The fitting parameter is  $g \approx 0.02$ . Letters in the picture correspond to those in Fig. 5. (b) The Rabi frequency extracted from (a) vs the applied UHF amplitude. The straight line is the predicted dependence  $\omega_R/\omega_T = \sqrt{P/P_0}$ . The good agreement provides strong evidence for Rabi oscillations.

Microwave irradiation (UHF signal) was introduced to the sample by a commercial coaxial cable (between room temperature and  $\sim 2$  K) and the resistive coaxial cable, known as ThermoCoax (between  $\sim 2$  K and 10 mK). In order to reduce external disturbances, a 20 dB commercial attenuator was installed at 2 K. To measure  $S_V$ , we tuned the UHF signal in resonance with the qubit level separation. We found noticeable output signal only when  $\omega_{\text{HF}}/2\pi = 868 \pm 2$  MHz, in agreement with the estimated splitting  $\Delta/h \sim 1$  GHz. Note that there is a difference of two orders of magnitude between  $\omega_{\text{HF}}$  and the readout frequency  $\omega_T$ . Together with the high  $Q_T$ , this ensures that the signal can only be due to resonant transitions in the qubit itself. This was verified by measuring  $S_V$  when biasing the qubit away from degeneracy. A signal exceeding the background, that is, emission of  $\sim 6$  MHz photons by the qubit in response to a resonant UHF field in agreement with Eq. (24), was only detected when the qubit states were almost degenerate (cf. below Eq. (22)). The measurements were carried out at nominal temperature  $T = 10$  mK. No effect of radiation was observed above 40 mK (with  $40 \text{ mK}/hk_B \approx 830$  MHz, i.e. close to  $\Delta/h$ ). We plotted  $S_V(\omega)$  for different HF powers  $P$  in Fig. 5. As  $P$  is increased,  $\omega_R$  grows and passes  $\omega_T$ , leading to a non-monotonic dependence of the maximum signal on  $P$  in agreement with the above picture. This and the sharp dependence on the tuning of  $\omega_{\text{HF}}$  to the qubit frequency confirm that the effect is due to Rabi oscillations.

For a quantitative comparison between theory and experiment, we subtracted the measured signal without an HF power from the observed  $S_V$ , yielding the qubit's contribution  $S_{VQ} = S_V - S_{VT}(\omega)$ . Subsequently, we extracted the peak values vs. UHF amplitude,  $S_{VQ,max}(\sqrt{P/P_0}) = \max_{\omega} S_{VQ}(\omega) \approx S_{VQ}(\omega_T)$ , where  $P_0$  is the power causing the maximum response; see Fig. 6a. In the same figure, we plot the theoretical curve

for  $S_{VQ,\max}$  normalized to its maximum  $S_0$ ,

$$\frac{S_{VQ,\max}(w)}{S_0} = \frac{w^2 g^2}{(w^2 - 1)^2 + g^2} \approx \frac{(g/2)^2}{(w-1)^2 + (g/2)^2}; \quad (25)$$

$w \equiv \Omega_R/\omega_T$  ( $= \sqrt{P/P_0}$  theoretically) and  $g = \Gamma/\omega_T$ . The best fit is found for  $\Gamma \approx 0.02 \omega_T \sim 8 \cdot 10^5 \text{ s}^{-1}$ . Thus, the life-time of the Rabi oscillations is at least  $\tau_{\text{Rabi}} = 2/\Gamma \approx 2.5 \mu\text{s}$ , leading to an effective quality factor  $Q_{\text{Rabi}} = \Delta/(\hbar\Gamma) \sim 7000$ . These values substantially exceed those obtained recently for a modified 3JJ qubit ( $\tau_{\text{Rabi}} \sim 150\text{ns}$ ),<sup>22</sup> which is not surprising. In our setup the qubit is read out not with a dissipative DC-SQUID, but with a high-quality resonant tank. The latter is weakly coupled to the qubit ( $k^2 \sim 10^{-3}$ ), suppressing the noise leakage to it.<sup>25</sup>

#### IV. RESONANT SPECTROSCOPY

In this section we show that the IMT can be also used for resonant spectroscopy, which is a well-known experimental method for investigation of quantum systems. As an example of such IMT application let us consider an interferometer-type charge qubit.<sup>26,27,28</sup> The device's core element is a single-Cooper-pair transistor - a small island, separated by two mesoscopic Josephson junctions, which is capacitively coupled to the gate. The transistor can be described by the Hamiltonian matrix<sup>29,30</sup>

$$H_{nm} = 4E_C(N - n_g)^2 \delta_{nm} - \frac{\varepsilon_J(\varphi)}{2} (\delta_{n,m+1} + \delta_{n,m-1}) \quad (26)$$

where  $N$  is number of Cooper pairs on the island,  $\delta_{n,m}$  is Kronecker symbol,  $E_C = e^2/2C_\Sigma$  is the single-electron charging energy expressed through the total island capacitance  $C_\Sigma$ . The dimensionless parameter  $n_g = C_g V_g/2e$  is continuously controllable by the gate voltage  $V_g$  via the capacitance  $C_g$ . The effective Josephson energy

$$\varepsilon_J(\varphi) = [E_{J1}^2 + E_{J2}^2 + 2E_{J1}E_{J2} \cos \varphi]^{1/2}, \quad (27)$$

is a function of the total phase difference across both junctions  $\varphi = \phi_1 + \phi_2$ , where  $E_{J1,J2}$  and  $\phi_{1,2}$  are Josephson coupling energies and phase differences of the first and second junction, respectively.

If the transistor is closed by a superconducting loop with low inductance  $L_q$ , the total phase difference is  $\phi \approx 2\pi\Phi_e/\Phi_0$  and the ground-state curvature  $d^2 E_-/d\Phi_e^2$  can be obtained finding smallest eigenvalue of the Hamiltonian matrix (26) as a function of  $\Phi_e$ . Using (3), we can calculate the phase shift of the tank inductively coupled to the charge qubit and compare it with experimental results obtained by IMT.<sup>32</sup> The principle of resonant spectroscopy is very simple. If the qubit is irradiated by microwaves with frequency corresponding to the energy gap between ground ( $n=0$ ) and upper level ( $n=1$ ) the latter one becomes also populated. In this sense the microwave

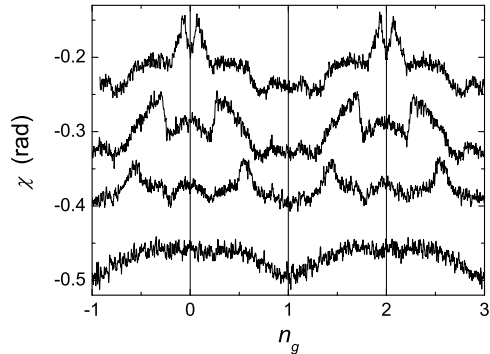


FIG. 7: Tank phase shift  $\chi$  vs. gate parameter  $n_g$  without microwave power (lowest curve) and with microwave power at different excitation frequencies. The data correspond to  $\omega_{UHF}/2\pi = 8.9, 7.5, 6.0$  GHz (from top to bottom). The magnetic flux  $\Phi_e = \Phi_0/2$  threading the interferometer loop provides a total phase difference  $\delta = \pi$  across the single-Cooperpair transistor. (For clarity, the upper curves are shifted.)

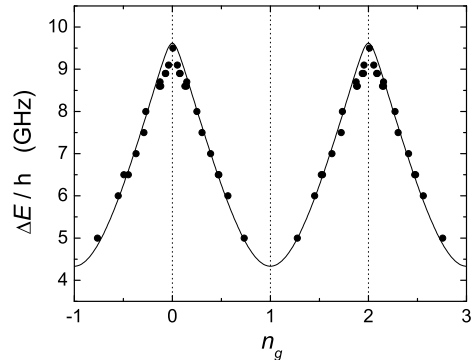


FIG. 8: Energy gap  $\Delta$  between the ground and upper bands of the transistor determined from the experimental data for the case  $\delta = \pi$ . Some examples of these data are shown in Fig. 7. Dots represent the experimental data, the solid line corresponds to the fit (cf. text).

irradiation acts like temperature i.e. suppresses the tank phase shift (see Eq.18).

Similar to the phase qubits, the interferometer-type charge qubit was fabricated out of Al by the conventional shadow evaporation technique, and was placed in the middle of the Nb coil by making use of a flip-chip configuration. The geometric loop inductance of the interferometer was calculated to be  $L_q = 0.8$  nH. The layout size of the junctions was 140 nm x 180 nm. Deviations from the nominal dimensions caused by the fabrication process were estimated from the micrograph of the real structure and found to be less than 15 %. The charging energy was overestimated within the framework of the plate capacitor model from the junctions delivering

$E_C \simeq 7$  GHz. In fact and also in accordance with the experimental results below, this value is reduced due to the strong tunneling regime.<sup>31</sup> The measurements were performed at mixing chamber temperature of 10 mK.

The presence of the microwave power significantly changes the obtained dependence, namely peaks appear in the  $\chi(n_g)$  curve (see upper curves in Fig. 7). The peak position depends on the microwave frequency and does not depend on the amplitude (shape slightly depends). These peaks disappear when the phase bias is far from  $\pi$  as well as at higher temperatures. Therefore, we believe, that they correspond to the excitation of the system from the ground to the upper state.

The microwave induced transition (both the frequency of the microwave and the phase difference across the transistor  $\varphi = \pi$  are fixed) from the ground to the upper state occurs only at certain value of the gate charge. From the position of the peaks on the  $\chi(n_g)$  curves at different frequencies of the microwave, we have reconstructed the energy difference between ground and upper states as a function of the quasicharge on the island. The obtained dependence is shown in Fig. 8. We fitted the experimental data by using the numerical solution of the energy spectrum of the Hamiltonian matrix (26). The best fitting parameters were found to be  $\varepsilon_J(\pi) = 4.4$  GHz and  $E_C = 2.2$  GHz. This value of the Josephson coupling energy is in very good agreement with the estimated value, and, as expected, the charging energy is smaller than estimated.

## V. NONRESONANT SPECTROSCOPY OF TWO COUPLED QUBITS

After the successful demonstration of quantum coherence in many types of superconducting qubits an observation of entangled states in two coupled qubits presents the next step on the road to the quantum processor. The entangled states were recently observed in both the charge<sup>33</sup> and the current-biased Josephson junction<sup>34</sup> qubits. In this section we demonstrate that entangled states in a system of two inductively coupled flux qubits<sup>35</sup> can be detected by the IMT.<sup>36</sup>

The system of two flux Al qubits inductively coupled to each other and to the Nb tank is shown in Fig. 9. The area of each qubit and self-inductance, and critical current were  $S_q = 80 \mu\text{m}^2$ ,  $L_q = 39$  pH,  $I_c \approx 400$  nA, and  $E_C \approx 3.2$  GHz, respectively. The mutual inductance between the qubits  $M_{ab} = 2.7$  pH was estimated numerically from the electron micrograph. The magnetic flux through the qubits was created by the dc component of the current in the coil  $I_{dc1}$  and by the bias current  $I_{dc2}$  through a wire close to one of the qubits. This allowed independent control of the bias in each qubit. The system of Fig. 9 is described by the Hamiltonian  $H = H_0 + H_T + H_{int} + H_{diss}$ , where the two-qubit Hamiltonian in the two-state approximation is expressed as<sup>8</sup>

$$H_0 = -\Delta_a \sigma_x^{(a)} - \Delta_b \sigma_x^{(b)} + \epsilon_a \sigma_z^{(a)} + \epsilon_b \sigma_z^{(b)} + J \sigma_z^{(a)} \sigma_z^{(b)}, \quad (28)$$

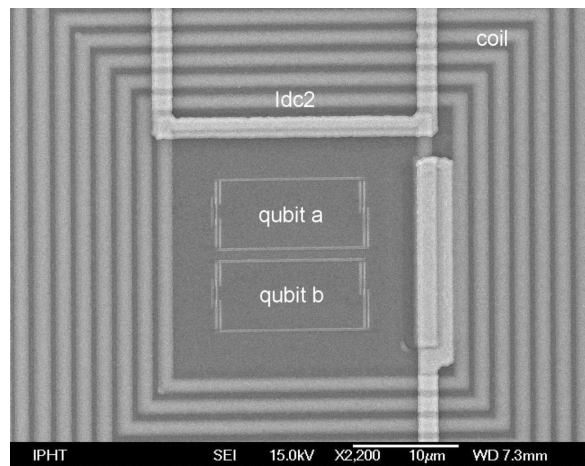


FIG. 9: Micrograph of the two-qubit system coupled to a resonant tank circuit.

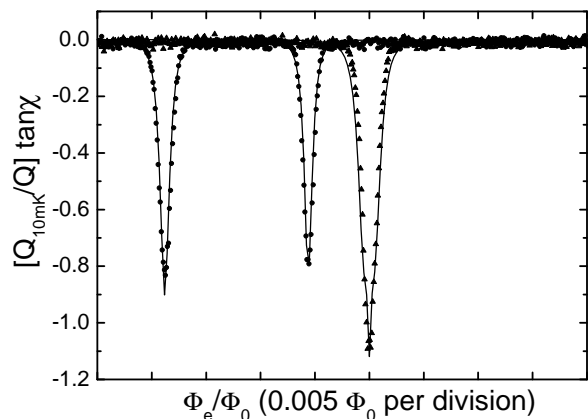


FIG. 10: Normalized tangent of the current-voltage angle  $\chi$  in the tank vs. external flux bias  $\Phi_e$  at 50 mK. A relative flux bias  $f_{shift}$  between the qubits is created by changing the current  $I_{dc2}$  in the additional wire. The shifted curves correspond to  $I_{dc2} = 27.3 \mu\text{A}$ , while the central curve is for  $I_{dc2} = -2.7 \mu\text{A}$ . The experimental data are denoted by the dots ( $I_{dc2} = 27.3 \mu\text{A}$ ) and triangles ( $I_{dc2} = -2.7 \mu\text{A}$ ). Solid curves correspond to theoretical fitting.

$H_T$  is the tank Hamiltonian (a harmonic oscillator), the qubit-tank interaction is

$$H_{int} = -(\lambda_a \sigma_z^{(a)} + \lambda_b \sigma_z^{(b)}) I_T, \quad (29)$$

and  $H_{diss}$  describes the standard weak coupling of the qubits to a dissipative bath<sup>37</sup>.

Here the coefficients are  $\lambda_{a/b} = M_{a/b,T} I_{a/b}$ , where  $M_{a/b,T}$  is the qubit-tank mutual inductance,  $L_{a/b}$  is the self-inductance and  $I_{a/b}$  is the amplitude of the persistent current in the corresponding qubit. In the standard two-state approximation, the qubit current operators are  $\hat{I}_{a/b} = I_{a/b} \sigma_z^{(a/b)}$ . The qubit biases are given by  $\epsilon_a = I_a \Phi_0 (f_x - 0.5 + f_{shift})$ ,  $\epsilon_b = I_b \Phi_0 (f_x - 0.5 + \eta f_{shift})$ , where the dimensionless flux  $f_x \sim I_{dc1}$  describes the field created by the niobium coil in both qubits, while the pa-



parameters  $f_{\text{shift}} \sim I_{dc2}$  and  $\eta = M_{bw}/M_{aw} < 1$  give the bias difference between the qubits created by the additional wire. Here  $M_{aw}$  ( $M_{bw}$ ) are the mutual inductances between the  $a$  ( $b$ ) qubit and the additional dc wire (for our sample,  $M_{aw}$  and  $M_{bw}$  were calculated numerically, yielding  $\eta = 0.32$ ). The qubit–qubit coupling constant  $J = M_{ab}I_aI_b$  is positive because the two qubits are in the same plane side to side, leading to antiferromagnetic coupling (according to the north-to-south attraction law).

The application of the IMT for spectroscopy of two coupled qubits, similar to single-qubit problem (see section II), can be conveniently discussed in terms of their magnetic susceptibility  $\chi_{zz}$ . In the linear-response approximation the magnetic susceptibility of the two-qubit system  $\chi_{zz}(\omega)$  is expressed through retarded Green's functions of the qubit operators  $\sigma_z^{(a/b)}$ , calculated with the equilibrium density matrix  $\rho = e^{(F-H_0)/T}$  with  $H_0$  as in Eq. (28). It can be generally assumed that the latter's eigenvalues  $E_\mu$ ,  $\mu = 1, 2, 3, 4$ , are non-degenerate and the eigenstates are orthonormalized,  $\langle \nu | \mu \rangle = \delta_{\mu\nu}$ . Taking into account the qubits' interaction with a dissipative environment,<sup>17,38</sup> we derive

$$\chi_{zz}(\omega) = - \sum_{\mu \neq \nu} \frac{\rho_\mu - \rho_\nu}{\omega + E_\mu - E_\nu + i\Gamma_{\mu\nu}} P_{\mu\nu}, \quad (30)$$

$$\tan \chi = -2 \frac{Q_T}{L_T} \sum_{\mu < \nu} \frac{\rho_\mu - \rho_\nu}{E_\nu - E_\mu} P_{\mu\nu}, \quad (31)$$

where  $\rho_\mu = \exp(-E_\mu/T)/Z$  is a thermal population of the  $\mu$  energy level,  $Z = \sum_\nu \exp(-E_\nu/T)$ ,  $\Gamma_{\mu\nu}$  are decoherence rates of the double-qubit system, and

$$\begin{aligned} P_{\mu\nu} = & \lambda_a^2 \langle \mu | \sigma_z^{(a)} | \nu \rangle \langle \nu | \sigma_z^{(a)} | \mu \rangle + \lambda_b^2 \langle \mu | \sigma_z^{(b)} | \nu \rangle \langle \nu | \sigma_z^{(b)} | \mu \rangle \\ & + \lambda_a \lambda_b \langle \mu | \sigma_z^{(a)} | \nu \rangle \langle \nu | \sigma_z^{(b)} | \mu \rangle \\ & + \lambda_a \lambda_b \langle \mu | \sigma_z^{(b)} | \nu \rangle \langle \nu | \sigma_z^{(a)} | \mu \rangle. \end{aligned} \quad (32)$$

At low frequencies  $\omega = \omega_T \ll |E_\mu - E_\nu|$  and in a weak damping regime,  $\Gamma_{\mu\nu} \ll |E_\mu - E_\nu|$ , the decoherence rates  $\Gamma_{\mu\nu}$  have no effect on  $\tan \chi$ , but are responsible for an equilibrium distribution in the system.

The first two terms in Eq. (32) are non-zero even if the two-qubit states are factorized. The first (second) term corresponds to the contribution of qubit  $a$  ( $b$ ) and is nonzero near the qubit's degeneracy point. These contributions are practically independent of whether the qubits' degeneracy points coincide or not.

The second and third lines in Eq. (32) describe coherent flipping of both qubits, which is *only* possible for non-factorizable (entangled) eigenstates  $|\mu\rangle$ ,  $|\nu\rangle$ . Therefore the difference between the coinciding IMT dip of the

two qubits and the sum of two single-qubit IMT dips provides a measure of how coherent is the two-qubit dynamics (that is, whether entangled eigenstates of the two-qubit Hamiltonian Eq. (28) are formed). This is a necessary condition for the system to be in an entangled (pure or mixed) state.

The measurement results are shown in Fig. 10. Comparison of the single-qubit dips with the coincident IMT dip shows clearly that the contribution to  $\tan \chi$  from the entangled eigenstates is significant. Indeed, the amplitude of the central dip in Fig. 10 at  $T = 50$  mK is 1.12, compared to the sum of the single-qubit dips equal to 1.69. It means that the entangled terms (second and third lines in Eq. (32)) are responsible for the negative contribution  $\approx -0.57$  to  $\tan \chi$ .

At 50 mK the temperature is comparable to the characteristic energies in the two-qubit system (at the two-qubit degeneracy point the gap between the ground state and top excited state is  $\sim 100$  mK). Since the characteristic measurement time in our approach is dictated by the much smaller tank frequency,  $\omega_T$ , the system will have time to equilibrate. Indeed, an excellent quantitative agreement between the experiment (Fig. 10) and the theory Eq. (31) confirms that the system is described by the equilibrium density matrix with the Hamiltonian Eq. (28) (all the parameters of which we determined from the experiment). In other words, our system is in an equilibrium mixture of entangled two-qubit states.

## VI. SUMMARY

We have shown that interferometer-type superconducting qubits can be characterized by making use of the impedance measurement technique. Moreover, weak continuous quantum measurements can be performed with this method.

## VII. ACKNOWLEDGMENTS

We are grateful to our colleagues M. H. S. Amin, Ya. S. Greenberg, H. E. Hoenig, U. Hübner, A. Maassen van den Brink, T. May, V. I. Shnyrkov, and I. N. Zhilyaev for their help and contribution to this work on different stages.

Helpful discussions with D. V. Averin, G. Blatter, M. Feigel'man, M. V. Fistul, V. B. Geshkenbein, A. J. Leggett, Yu. Makhlin, A. N. Omelyanchouk, A. Shnirman, P. C. E. Stamp, S. Uchaikin, A. V. Ustinov, A. D. Zaikin, and A. B. Zorin are gratefully acknowledged.

---

\* Electronic address: ilichev@ipht-jena.de

<sup>1</sup> D.V. Averin in *Quantum noise in mesoscopic physics*,

- edited by Yu.V. Nazarov (Kluwer 2003).
- <sup>2</sup> A.O. Caldeira and A.J. Leggett *Ann. Phys. (N.Y.)* **149**, 374 (1983).
  - <sup>3</sup> J. Clarke, A.N. Cleland, M.H. Devoret, D. Esteve, and J.M. Martinis, *Science* **239**, 992 (1988).
  - <sup>4</sup> R. Rouse, S. Han, and J.E. Lukens, *Phys. Rev. Lett.*, **75**, 1614 (1995).
  - <sup>5</sup> J.R. Friedman, V. Patel, W. Chen, S.K. Tolpygo, and J.E. Lukens, *Nature* **406**, 43 (2000).
  - <sup>6</sup> C.H. van der Wal, A.C.J. ter Haar, F.K. Wilhelm, R.N. Schouten, C.J.P.M. Harmans, T.P. Orlando, S. Lloyd, and J.E. Mooij, *Science* **290**, 773 (2000).
  - <sup>7</sup> J.E. Mooij, T.P. Orlando, L. Levitov, L. Tian, C.H. van der Wal, and S. Lloyd, *Science* **285**, 1036 (1999).
  - <sup>8</sup> A. Maassen van den Brink, cond-mat/0310425.
  - <sup>9</sup> L.D. Landau, *Z. Phys. Sowjetunion* **2**, 46 (1932); C. Zener, *Proc. R. Soc. London A* **137**, 696 (1932).
  - <sup>10</sup> E. Il'ichev, Th. Wagner, L. Fritzsche, J. Kunert, V. Schultze, T. May, H. E. Hoenig, H.G. Meyer, M. Grajcar, D. Born, W. Krech, M. V. Fistul, and A. M. Zagoskin, *Appl. Phys. Lett.* **80**, 4184 (2002).
  - <sup>11</sup> A. H. Silver and J. E. Zimmerman, *Phys. Rev. B* **157**, 317 (1967).
  - <sup>12</sup> N. Oukhanski, M. Grajcar, E. Il'ichev, and H.-G. Meyer, *Rev. Sci. Instr.* **74**, 1145 (2003).
  - <sup>13</sup> A. Izmalkov, M. Grajcar, E. Il'ichev, N. Oukhanski, Th. Wagner, H.-G. Meyer, W. Krech, M.H.S. Amin, Alec Maassen van den Brink, A.M. Zagoskin, *Europhys. Lett.* **65**, 844 (2004).
  - <sup>14</sup> E. Il'ichev, V. Zakosarenko, L. Fritsch. R. Stolz, H.E. Hoenig, H.-G. Meyer, M. Götz, A.B. Zorin, V.V. Khanin, A.B. Pavolotsky, and J. Niemeyer, *Rev. Sci. Instr.* **72**, 1882 (2001).
  - <sup>15</sup> Ya.S. Greenberg, A. Izmalkov, M. Grajcar, E. Il'ichev, W. Krech, H.-G. Meyer, M.H.S. Amin, and A. Maassen van den Brink, *Phys. Rev. B* **66**, 214525 (2002).
  - <sup>16</sup> M. Grajcar, A. Izmalkov, E. Il'ichev, Th. Wagner, N. Oukhanski, U. Hübner, T. May, I. Zhilyaev, H.E. Hoenig, Ya.S. Greenberg, V.I. Shnyrkov, D. Born, W. Krech, H.-G. Meyer, Alec Maassen van den Brink, and M.H.S. Amin, *Phys. Rev. B* **69**, 060501 (R) (2004).
  - <sup>17</sup> A.Yu. Smirnov, *Phys. Rev. B* **68**, 134514 (2003).
  - <sup>18</sup> The fact that  $\tan \chi$  is proportional to the magnetic susceptibility was already used for investigation of the magnetic response of "classical" Josephson samples - see E. Il'ichev, F. Tafuri, M. Grajcar, R.P.J. IJsselsteijn, J. Weber, F. Lombardi, and J.R. Kirtley, *Phys. Rev. B* **68**, 014510 (2003).
  - <sup>19</sup> Y. Nakamura, Yu.A. Pashkin, and J.S. Tsai, *Phys. Rev. Lett.* **87**, 246601 (2001).
  - <sup>20</sup> D. Vion, A. Aassime, A. Cottet, P. Joyez, H. Pothier, C. Urbina, D. Esteve, and M.H. Devoret, *Science* **296**, 886 (2002).
  - <sup>21</sup> J.M. Martinis, S. Nam, J. Aumentado, and C. Urbina, *Phys. Rev. Lett.* **89**, 117901 (2002).
  - <sup>22</sup> I. Chiorescu, Y. Nakamura, C.J.P.M. Harmans, and J.E. Mooij, *Science* **299**, 1869 (2003).
  - <sup>23</sup> J.M. Raimond, M. Brune, and S. Haroche, *Rev. Mod. Phys.* **73**, 565 (2001).
  - <sup>24</sup> A.Yu. Smirnov, *Phys. Rev. B* **67**, 155104 (2003).
  - <sup>25</sup> E. Il'ichev, N. Oukhanski, A. Izmalkov, Th. Wagner, M. Grajcar, H.-G. Meyer, A.Yu. Smirnov, Alec Maassen van den Brink, M.H.S. Amin, and A.M. Zagoskin, *Phys. Rev. Lett.* **91**, 097906 (2003).
  - <sup>26</sup> J.R. Freedman and D.V. Averin, *Phys. Rev. Lett.* **88**, 050403 (2002).
  - <sup>27</sup> A.B. Zorin, *Physica C* **368**, 284 (2002).
  - <sup>28</sup> W. Krech, M. Grajcar, D. Born, I. Zhilyaev, Th. Wagner, E. Il'ichev, and Ya. Greenberg, *Phys. Lett. A* **303**, 352 (2002).
  - <sup>29</sup> D.V. Averin and K.K. Likharev in *Mesoscopic Phenomena in Solids*, edited by B.L. Altshuler, P.A. Lee, and A. Webb (Elsevier, Amsterdam), 173, (1991).
  - <sup>30</sup> M. Tinkham, *Introduction to Superconductivity*, McGraw-Hill, New York (1996), p.276.
  - <sup>31</sup> A.I. Larkin and Yu.N. Ovchinnikov, *Phys. Rev. B* **28**, 6281 (1983); G. Schön and A.D. Zaikin, *Phys. Rep.* **198**, 237 (1990).
  - <sup>32</sup> D. Born, V.I. Shnyrkov, W. Krech, Th. Wagner, E. Il'ichev, U. Hübner, H.-G. Meyer, cond-mat/0312696.
  - <sup>33</sup> Yu.A. Pashkin, T. Yamamoto, O. Astafiev, Y. Nakamura, D.V. Averin, J.S. Tsai, *Nature* **421**, 823 (2003).
  - <sup>34</sup> A.J. Berkley, H. Xu, R.C. Ramos, M.A. Gubrid, F.W. Strauch, P.R. Johnson, J.R. Anderson, A.J. Dragt, C.J. Lobb, F.C. Wellstood, *Science* **300**, 1548 (2003).
  - <sup>35</sup> J.B. Majer, F.G. Paauw, A.C.J. ter Haar, C.J.P.M. Harmans, J.E. Mooij, cond-mat/0308192.
  - <sup>36</sup> A. Izmalkov, M. Grajcar, E. Il'ichev, Th. Wagner, H.-G. Meyer, A.Yu. Smirnov, M.H.S. Amin, Alec Maassen van den Brink, A.M. Zagoskin, cond-mat/0312332 (*Phys. Rev. Lett.*, to be published).
  - <sup>37</sup> U. Weiss, *Quantum Dissipative Systems*, 2nd edition (World Scientific, Singapore, 1999).
  - <sup>38</sup> A.Yu. Smirnov, cond-mat/0312635.